A 'magnetic' interatomic potential for molecular dynamics simulations

2005 J. Phys.: Condens. Matter 17 7097

(http://iopscience.iop.org/0953-8984/17/44/003)

INSTITUTE OF PHYSICS PUBLISHING JOURNAL OF PHYSICS: CONDENSED MATTER

J. Phys.: Condens. Matter **17** (2005) 7097–7118 doi:10.1088/0953-8984/17/44/003

A 'magnetic' interatomic potential for molecular dynamics simulations

S L Dudarev[1] **and P M Derlet**[2]

[1] EURATOM/UKAEA Fusion Association, Culham Science Centre, Oxfordshire OX14 3DB, UK
[2] Paul Scherrer Institute, CH-5232 Villigen PSI, Switzerland

E-mail: Sergei.Dudarev@UKAEA.org.uk and Peter.Derlet@psi.ch

Received 4 July 2005, in final form 8 September 2005
Published 17 October 2005
Online at stacks.iop.org/JPhysCM/17/7097

Abstract

We develop a semi-empirical many-body interatomic potential suitable for large scale molecular dynamics simulations of magnetic α-iron. The functional form of the embedding part of the potential is derived using a combination of the Stoner and the Ginzburg–Landau models. We show that it is the symmetry broken solutions of the Ginzburg–Landau model describing spontaneous magnetization of atoms that provide the link between magnetism and interatomic forces. We discuss a range of potential applications of the new method.

(Some figures in this article are in colour only in the electronic version)

1. Introduction

The significance of taking magnetic effects into account for the development of sufficiently accurate models of interatomic interactions in α-iron has recently been recognized as a problem, the resolution of which is essential for the development of predictive models of iron-based alloys and steels for fusion and advanced nuclear applications. For example, the authors of a recent comprehensive review of the currently available modelling methodologies [1] noted that '... the absence of a physically sensible treatment of magnetization points to more fundamental problems in the many-body potential concept'. The need to develop more accurate models of interatomic interactions for modelling radiation damage was also highlighted in a recent review of innovative materials for fusion power plant structures [2].

The fact that the presence of magnetism stabilizes the body-centred cubic (bcc) α-phase of iron was first noted by Hasegawa and Pettifor [3]. They showed that the entropy term associated with magnetic fluctuations in the face-centred cubic (fcc) phase was responsible for the phase transition from the bcc α to the fcc γ phase occurring at approximately 912 °C. The fact that the ferromagnetically ordered bcc phase of iron is more stable than any of the fcc phases was later confirmed by density functional theory (DFT) calculations carried out

using the generalized gradient approximation (GGA) [4–6]. A recent tight-binding study [7] also showed the significance of the magnetic contribution to the energy of interaction between atoms in α-iron. The fact that magnetism favours certain crystal structures may be interpreted as a manifestation of the effect of electron correlations on interatomic forces similar to that found in transition metal oxides using the LSDA + U method [8].

The accuracy of the density functional and tight-binding approaches is sufficient to identify effects associated with magnetic interactions in iron, but practically it proves impossible to extend these approaches to systems containing $\sim$100 000 atoms. Modelling systems of this size is necessary for understanding effects of long-range elastic interactions responsible for swelling, embrittlement and creep of materials under irradiation. Hence the development of phenomenological models suitable for fast evaluation of forces acting between atoms in a magnetic material is required for carrying out molecular dynamics simulations of thermally activated processes occurring in iron and iron-based alloys under irradiation. Density functional calculations have already confirmed the significance of a magnetic contribution to the energies of self-interstitial defects in iron [9–12], and these results now need to be extended to much larger systems in order to link simulations with experimental observations of properties of materials and for the interpretation of electron microscope images of defects.

The currently available semi-empirical atomistic models of ferromagnetic Fe are based on the many-body formalism [13–16] that was originally developed for the treatment of interatomic interactions in non-magnetic metals. A notable exception is a recent work by Ackland [17], who discussed several ways of including magnetic effects in the many-body potential formalism. In this paper we follow a route that was not considered in [17].

We develop a phenomenological many-body empirical potential model that treats the effect of magnetism on the energy of interaction between atoms in α-iron. Our approach is based on a combination of the Stoner and the Ginzburg–Landau models. The first describes correlation effects giving rise to the occurrence of magnetism in an electron gas and constitutes a relatively simple model for band magnetism that is able to describe the ground state properties of the ferromagnetic 3d transition metals [18], while the second represents the simplest model of a second order phase transition. We show that it is the symmetry broken solutions of the Ginzburg–Landau model describing spontaneous magnetization of atoms that are responsible for the link between magnetism and interatomic forces. In agreement with density functional and tight-binding calculations we find that the occurrence of magnetism in α-iron is closely related to the shape of the distribution of the density of electronic states. While the rectangular band model predicts the discontinuous formation of either a non-magnetic or a fully saturated magnetic configuration, numerical solutions based on the density functional or the tight-binding densities of states of iron, as well as an analytically solvable generalized parabolic band model, show that the magnetization curves are well approximated by the Ginzburg–Landau model. Using this approach, we derive a phenomenological embedding function of the many-body interatomic potential. By adjusting the effective pairwise density functions and pairwise interactions we parametrize the energy of interatomic interactions in a form that describes the equation of state *both* for the non-magnetic *and* magnetic configurations, and also the energies of vacancy and self-interstitial point defects in α-iron.

Our objective here is to make the first step in the development of a 'magnetic' interatomic potential rather than to present a model capable of encompassing all the available information about the structure and dynamical properties of all the phases of magnetic iron. Our approach extends the existing treatment of interatomic interactions, where the energy is described by a single-valued function of atomic coordinates, and links it with the concept of symmetry breaking, leading to *multi-branching* of the effective potential. Since in a magnetic system the energy depends not only on the position of atoms, but also on the configuration of magnetic

moments, the total energy is no longer given by a unique function of atomic coordinates. Instead, in a magnetic system we find that *several* energy surfaces correspond to the same geometric configuration of atoms. In the case considered below we only treat the ferromagnetic case where the energy surface consists of two (non-magnetic and ferromagnetic) sheets. However, at the expense of added complexity, our method can be generalized to the case of arbitrary magnetic configurations.

2. The band magnetism and the Ginzburg–Landau model

We start by considering the rectangular band model of cohesion in a transition metal. In this model, the density of single electronic states *per atom per spin* is given by

$$D(E) = \mathcal{N}/2W, \qquad -W/2 < E < W/2, \tag{1}$$

where W is the width of the band and $\mathcal{N} = 10$ is the total number of d orbitals per atom. The band energy per atom equals

$$E_{\mathrm{tot}} = E_{\uparrow} + E_{\downarrow} - I\zeta^2/4, \tag{2}$$

where $E_{\uparrow}$ and $E_{\downarrow}$ are the energies of spin up and spin down sub-bands, $\zeta = N_{\uparrow} - N_{\downarrow}$ is the magnetic moment of an atom, and I is the Stoner parameter. The equilibrium value of the magnetic moment is determined by the condition that the total energy of the system (2) is a minimum. The energies $E_{\uparrow}$ and $E_{\downarrow}$ of the filled majority and minority spin sub-bands are given by the integrals of the density of states up to the Fermi energies $\epsilon_{\mathrm{F}\uparrow}$ and $\epsilon_{\mathrm{F}\downarrow}$ of spin up and spin down electrons [19],

$$E_{\uparrow} = \int_{-\infty}^{\epsilon_{\mathrm{F}\uparrow}} E D(E)\,\mathrm{d}E, \qquad E_{\downarrow} = \int_{-\infty}^{\epsilon_{\mathrm{F}\downarrow}} E D(E)\,\mathrm{d}E. \tag{3}$$

Similarly, the band occupation numbers are

$$N_{\uparrow} = \int_{-\infty}^{\epsilon_{\mathrm{F}\uparrow}} D(E)\,\mathrm{d}E, \qquad N_{\downarrow} = \int_{-\infty}^{\epsilon_{\mathrm{F}\downarrow}} D(E)\,\mathrm{d}E. \tag{4}$$

Using the rectangular band model, we find

$$N_{\uparrow} = \frac{\mathcal{N}}{2W}\left(\epsilon_{\mathrm{F}\uparrow} + \frac{W}{2}\right), \qquad N_{\downarrow} = \frac{\mathcal{N}}{2W}\left(\epsilon_{\mathrm{F}\downarrow} + \frac{W}{2}\right), \tag{5}$$

and

$$E_{\uparrow} = \frac{\mathcal{N}}{4W}\left(\epsilon_{\mathrm{F}\uparrow} - \frac{W}{2}\right)\left(\epsilon_{\mathrm{F}\uparrow} + \frac{W}{2}\right), \qquad E_{\downarrow} = \frac{\mathcal{N}}{4W}\left(\epsilon_{\mathrm{F}\downarrow} + \frac{W}{2}\right)\left(\epsilon_{\mathrm{F}\downarrow} - \frac{W}{2}\right). \tag{6}$$

The total energy evaluated using the rectangular band model is therefore

$$E_{\mathrm{tot}} = \frac{W}{\mathcal{N}}\left[\left(N_{\uparrow} - \frac{\mathcal{N}}{2}\right)N_{\uparrow} + \left(N_{\downarrow} - \frac{\mathcal{N}}{2}\right)N_{\downarrow}\right] - \frac{I}{4}(N_{\uparrow} - N_{\downarrow})^2. \tag{7}$$

This energy can also be expressed as a function of magnetic moment ζ and the total number of electrons $N = N_{\uparrow} + N_{\downarrow}$, namely

$$E_{\mathrm{tot}}(N, \zeta) = -\frac{W}{2\mathcal{N}}N(\mathcal{N} - N) + \frac{1}{2}\left(\frac{W}{\mathcal{N}} - \frac{I}{2}\right)\zeta^2. \tag{8}$$

The requirement that the total energy is a minimum as a function of ζ gives rise to either a non-magnetic state with $N_{\uparrow} = N_{\downarrow}$ for $I < 2W/\mathcal{N}$, or to a fully saturated magnetic configuration for $I > 2W/\mathcal{N}$. The occurrence of a discontinuous transition between the two limiting cases has led to the idea proposed in [17] to replace the Stoner term $-I\zeta^2/4$ by a linear term of

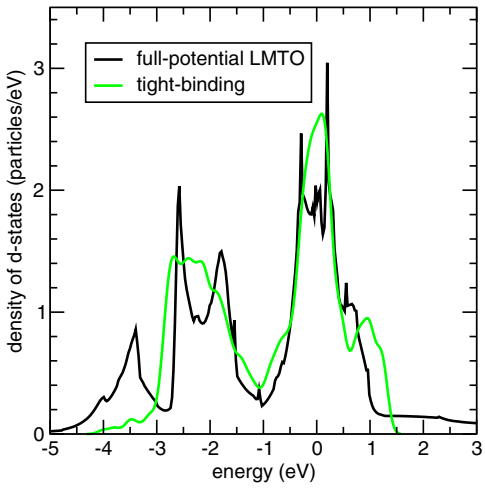

Figure 1. Distribution of the density of band electronic states $D(E)$ of the non-magnetic body-centred cubic iron. The black curve shows $D(E)$ calculated using the full-potential linearized muffin-tin orbital (LMTO) approach [38]. The grey curve was calculated using the tight-binding approximation developed in [7]. The total area under the curves is normalized to $\mathcal{N}/2 = 5$. In both cases the position of the Fermi energy corresponds to the origin of the energy axis.

the form $-E_0\zeta$, where E_0 is a phenomenological constant. Further terms linear in magnetic moment were also introduced to treat the effects of Pauli repulsion.

There are two reasons why terms linear in magnetic moment should not occur in the expression for the total energy. Firstly, the energy must remain invariant with respect to a change in the sign of the time variable [20]. Since the magnetic moment changes sign if time is reversed, the energy must be an even function of ζ. Terms linear in ζ enter the Hamiltonian only if an external magnetic field is present, in which case T-invariance is retained due to the fact that if time changes sign the directions of the magnetic moment *and* the magnetic field are reversed simultaneously [21]. The second point refers to the origin of the symmetry-breaking Stoner term $-I\zeta^2/4$. This term comes from the mean-field treatment of the Hubbard Hamiltonian [22, 23], which is quadratic in the electron occupation numbers and hence gives rise to a magnetic energy term quadratic in ζ. The Hubbard Hamiltonian describes the effect of on-site Coulomb repulsion between electrons or, in other words, strong electron–electron correlations that are also responsible for the ordering of many-body quantum states in a many-electron atom [24] and for the formation of bandgaps in Mott insulators [25].

We now show that the occurrence of a discontinuous magnetic phase transition in the rectangular band model noted above is not associated with the electron correlation (Stoner) term. Instead the nature of this discontinuity is related to the approximate treatment of the band contribution to the total energy[3].

Consider a general expression for the band energy of electrons, assuming that the density of states $D(E)$ has a form similar to that shown in figure 1, namely

$$E_{\rm tot}(N,\zeta) = \int_{-\infty}^{\epsilon_{\rm F\uparrow}} ED(E)\,{\rm d}E + \int_{-\infty}^{\epsilon_{\rm F\downarrow}} ED(E)\,{\rm d}E - I\zeta^2/4. \tag{9}$$

[3] In the case of body-centred cubic iron the rectangular band model does not approximate the actual distribution of the density of states sufficiently well. However, in other materials like face-centered cubic iron, the rectangular band model does provide a good approximation and this explains the rapid collapse of magnetic moment occurring under pressure, see [26].

This form is subject to the charge neutrality condition [27, 28] asserting that in a metal the total number of electrons per atom remains constant

$$N = \int_{-\infty}^{\epsilon_{F\uparrow}} D(E)\,\mathrm{d}E + \int_{-\infty}^{\epsilon_{F\downarrow}} D(E)\,\mathrm{d}E = \text{constant}. \tag{10}$$

The magnetic moment ζ is given by the difference between the occupation numbers of spin up and spin down states

$$\zeta = \int_{-\infty}^{\epsilon_{F\uparrow}} D(E)\,\mathrm{d}E - \int_{-\infty}^{\epsilon_{F\downarrow}} D(E)\,\mathrm{d}E = \int_{\epsilon_{F\downarrow}}^{\epsilon_{F\uparrow}} D(E)\,\mathrm{d}E. \tag{11}$$

Note that in equations (9)–(11) the Fermi energies $\epsilon_{F\uparrow} = \epsilon_{F\uparrow}(N,\zeta)$ and $\epsilon_{F\downarrow} = \epsilon_{F\downarrow}(N,\zeta)$ themselves are functions of the total number of electrons in the band N and the magnetic moment ζ. Since the equilibrium value of the magnetic moment is determined by the condition $\partial E/\partial\zeta = 0$, from equations (9)–(11) we find that *at equilibrium*

$$\begin{aligned}
&\epsilon_{F\uparrow} D(\epsilon_{F\uparrow})\frac{\partial\epsilon_{F\uparrow}}{\partial\zeta} + \epsilon_{F\downarrow} D(\epsilon_{F\downarrow})\frac{\partial\epsilon_{F\downarrow}}{\partial\zeta} - \frac{1}{2}I\zeta = 0\\
&D(\epsilon_{F\uparrow})\frac{\partial\epsilon_{F\uparrow}}{\partial\zeta} + D(\epsilon_{F\downarrow})\frac{\partial\epsilon_{F\downarrow}}{\partial\zeta} = 0\\
&D(\epsilon_{F\uparrow})\frac{\partial\epsilon_{F\uparrow}}{\partial\zeta} - D(\epsilon_{F\downarrow})\frac{\partial\epsilon_{F\downarrow}}{\partial\zeta} = 1.
\end{aligned} \tag{12}$$

By combining these equations we find a condition that relates the Fermi energies of the spin up and spin down sub-bands to the *equilibrium* value of the magnetic moment

$$\zeta = \frac{\epsilon_{F\uparrow}(N,\zeta) - \epsilon_{F\downarrow}(N,\zeta)}{I}. \tag{13}$$

Using the above definition (11) of ζ, equation (13) can also be represented in the form [29]

$$I\frac{\int_{\epsilon_{F\downarrow}}^{\epsilon_{F\uparrow}} D(E)\,\mathrm{d}E}{\left[\epsilon_{F\uparrow}(N,\zeta) - \epsilon_{F\downarrow}(N,\zeta)\right]} = I\langle D(E)\rangle = 1, \tag{14}$$

where $\langle D(E)\rangle$ is the density of states averaged over the interval of energies between $\epsilon_{F\downarrow}(N,\zeta)$ and $\epsilon_{F\uparrow}(N,\zeta)$.

At a minimum point the second order derivative of the total energy with respect to magnetic moment $\partial^2 E_{\mathrm{tot}}/\partial\zeta^2$ is positive. Evaluating the second derivative of (9) at the minimum point of $E_{\mathrm{tot}}(N,\zeta)$ we find

$$\frac{1}{2}\left[\frac{1}{D(\epsilon_{F\downarrow})} + \frac{1}{D(\epsilon_{F\uparrow})}\right] - I > 0. \tag{15}$$

This inequality can also be written in the form $\overline{D^{-1}(\epsilon)} - I > 0$, where $\overline{D^{-1}(\epsilon)} \equiv \overline{1/D(\epsilon)}$ is the average of the inverted non-magnetic density of states per spin between the two energies corresponding to a band-filling of $N_\uparrow$ and $N_\downarrow$, respectively. Note the difference between this equation and the Stoner criterion of magnetic instability $[1/D(\epsilon_F)] - I < 0$. The Stoner criterion describes an instability occurring at the point $\zeta = 0$ where the function $E_{\mathrm{tot}}(\zeta)$ is at a maximum. At the same time, condition (15) refers to a *stable* symmetry-broken magnetic configuration corresponding to a minimum of the function $E_{\mathrm{tot}}(N,\zeta)$ at a point where ζ is a solution of equations (13) or (14).

The fact that according to equation (13) the Fermi energies of spin up and spin down electrons are different does not imply the difference between the *chemical potentials* of spin

up and spin down electrons. Indeed, the chemical potentials of the majority and minority spin electrons are given by the derivatives

$$\mu_\uparrow = \frac{\partial E(N,\zeta)}{\partial N_\uparrow}, \qquad \mu_\downarrow = \frac{\partial E(N,\zeta)}{\partial N_\downarrow}. \tag{16}$$

Using the definitions $N_\uparrow = (N+\zeta)/2$ and $N_\downarrow = (N-\zeta)/2$, and taking into account that at a minimum $\partial E/\partial\zeta = 0$, we write

$$\begin{aligned} \frac{\partial E(N,\zeta)}{\partial N_\uparrow} &= \frac{\partial E}{\partial N}\frac{\partial N}{\partial N_\uparrow} + \frac{\partial E}{\partial \zeta}\frac{\partial \zeta}{\partial N_\uparrow} = \frac{\partial E}{\partial N} + \frac{\partial E}{\partial \zeta} = \frac{\partial E}{\partial N}, \\ \frac{\partial E(N,\zeta)}{\partial N_\downarrow} &= \frac{\partial E}{\partial N}\frac{\partial N}{\partial N_\downarrow} + \frac{\partial E}{\partial \zeta}\frac{\partial \zeta}{\partial N_\uparrow} = \frac{\partial E}{\partial N} - \frac{\partial E}{\partial \zeta} = \frac{\partial E}{\partial N}. \end{aligned} \tag{17}$$

These equations show that

$$\mu_\uparrow = \frac{\partial E(N,\zeta)}{\partial N_\uparrow} = \frac{\partial E(N,\zeta)}{\partial N} = \frac{\partial E(N,\zeta)}{\partial N_\downarrow} = \mu_\downarrow. \tag{18}$$

To find the actual value of the chemical potential of electrons we differentiate equations (9)–(11) with respect to N. Noting that N and ζ are independent variables, we write

$$\begin{aligned} &\epsilon_{\mathrm{F}\uparrow} D(\epsilon_{\mathrm{F}\uparrow})\frac{\partial \epsilon_{\mathrm{F}\uparrow}}{\partial N} + \epsilon_{\mathrm{F}\downarrow} D(\epsilon_{\mathrm{F}\downarrow})\frac{\partial \epsilon_{\mathrm{F}\downarrow}}{\partial N} = \mu \\ &D(\epsilon_{\mathrm{F}\uparrow})\frac{\partial \epsilon_{\mathrm{F}\uparrow}}{\partial N} + D(\epsilon_{\mathrm{F}\downarrow})\frac{\partial \epsilon_{\mathrm{F}\downarrow}}{\partial N} = 1 \\ &D(\epsilon_{\mathrm{F}\uparrow})\frac{\partial \epsilon_{\mathrm{F}\uparrow}}{\partial N} - D(\epsilon_{\mathrm{F}\downarrow})\frac{\partial \epsilon_{\mathrm{F}\downarrow}}{\partial N} = 0. \end{aligned} \tag{19}$$

Using these equations, we find the chemical potential

$$\mu = \frac{\partial E(N,\zeta)}{\partial N} = (\epsilon_{\mathrm{F}\uparrow} + \epsilon_{\mathrm{F}\downarrow})/2, \tag{20}$$

which has the same value for spin up and spin down electrons.

We now investigate how the magnetic part $E_{\mathrm{tot}}(N,\zeta) - E_{\mathrm{tot}}(N,0)$ of the total energy (9) varies as a function of magnetic moment ζ. Using the densities of states shown in figure 1 and solving equations (9)–(11) numerically, we find that the function $E_{\mathrm{tot}}(N,\zeta) - E_{\mathrm{tot}}(N,0)$ follows the curves shown by the dark solid lines in figure 2. We see that the total energy is an even function of magnetic moment ζ and it has two symmetrical minima at $\zeta \approx \pm 2.26\ \mu_{\mathrm{B}}$. While the equilibrium value of the magnetic moment depends on the magnitude of the Stoner parameter I, the two-well structure of the curve $E_{\mathrm{tot}}(N,\zeta) - E_{\mathrm{tot}}(N,0)$ represents an inherent property of the model. The presence of *two* minima in figure 2 is significant since they reflect the fact that in a ferromagnet the choice of the direction of magnetization is arbitrary and that the energy of a magnetic state is independent of whether the moment is pointing 'up' or 'down'.

The characteristic double-well shape of the curves shown in figure 2, as well as the fact that these curves describe the occurrence of spontaneous magnetization or, in other words, a magnetic phase transition, suggests that it might be possible to approximate the behaviour of the total energy treated as a function of ζ by means of a simple phenomenological parametrization of the function $E_{\mathrm{tot}}(N,\zeta)$. The simplest model of a second-order phase transition is the Ginzburg–Landau model [30], where the magnetic part of the total energy is represented by a sum of a second-order and a *positive* fourth-order term

$$E_{\mathrm{tot}}(N,\zeta) - E_{\mathrm{tot}}(N,0) = \alpha\zeta^2 + \beta\zeta^4. \tag{21}$$

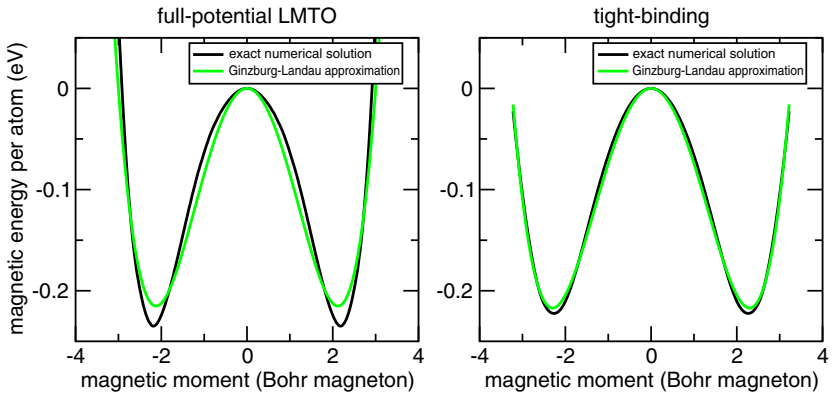

Figure 2. The magnetic part of the total energy $E_{\rm tot}(\zeta)$ calculated numerically using equations (9)–(11) and plotted as a function of magnetic moment ζ. Calculations based on the LMTO density of states were performed assuming that $I = 0.78$ eV and $N = 6.57$. The coefficients α and β of the Ginzburg–Landau model $E_{\rm tot}(\zeta) = \alpha\zeta^2 + \beta\zeta^4$ shown by the grey line are $\alpha = -9.55 \times 10^{-2}$ eV and $\beta = 1.06 \times 10^{-2}$ eV. Calculations based on the tight-binding density of states were performed assuming that $I = 0.66$ eV and $N = 6.76$. The coefficients α and β of the Ginzburg–Landau model fitted to the tight-binding solution are $\alpha = -8.22 \times 10^{-2}$ eV and $\beta = 7.78 \times 10^{-3}$ eV. The fact that in both cases we find that coefficient α is negative confirms that the non-magnetic configuration of bcc iron is unstable. This instability gives rise to the formation of a symmetry broken magnetic configuration with $\zeta \approx \pm 2.26\ \mu_{\rm B}$.

How well are the solutions of equations (9)–(11) approximated by this model? To answer this question, in figure 2 we plotted curves $\alpha\zeta^2 + \beta\zeta^4$ where coefficients α and β were chosen to provide the best fit to the exact numerical solutions of equations (9)–(11). Figure 2 shows that both the characteristic double-well structure of the curves and their numerical values agree well with the numerical solutions of equations (9)–(11). This suggests that the Ginzburg–Landau model, which is a simple analytically solvable model of a magnetic phase transition, provides an accurate approximation to the dependence of the total energy of a system of interacting magnetic atoms on their local environment even if the density of states $D(E)$ characterizing the electronic structure of the material exhibits the fairly complex behaviour illustrated in figure 1. Since the Ginzburg–Landau model provides an *explicit* expression for the magnetic contribution to the total energy, namely

$$E_{\rm tot}(N, \zeta)|_{\rm min} - E_{\rm tot}(N, 0) = -\frac{\alpha^2}{4\beta}, \tag{22}$$

where we assumed that $\alpha < 0$, the problem of finding the magnetic part of the many-body 'interaction potential' is reduced to determining how coefficients α and β depend on the local environment of a given atom. The fact that the Ginzburg–Landau model agrees well with the numerical solution of equations (9)–(11) shows that the universal form (21) may prove useful in evaluating the magnetic part of the total energy even within the framework of a fairly complex model of interatomic interactions (for example, a model based on the fourth-order recursion expansion [29]).

While this opens an interesting line of future work, in this paper we concentrate on the development of the simplest possible model of interatomic interaction suitable for carrying out molecular dynamics simulations of a magnetic material. In the following section we consider an analytically solvable *generalized* parabolic model of the density of states. This model on the one hand illustrates the formalism based on equations (9)–(11) and on the other hand makes

it possible to construct a working semi-empirical potential suitable for large-scale molecular dynamics simulations of a system of interacting magnetic atoms.

3. The semi-empirical magnetic potential

In the preceding section we showed that the requirement that the total energy $E_{\rm tot}(N,\zeta)$ must be an even function of magnetic moment is equivalent to the requirement that the Hamiltonian of the system is T-invariant. The Ginzburg–Landau model (21) containing both the second- and the fourth-order terms satisfies the T-invariance principle. At the same time, the fact that the Stoner term is quadratic in ζ and that the magnetic part of the band energy calculated using the rectangular band model (8) is also quadratic in ζ shows that in the rectangular band model we have no means for introducing the fourth-order term. While in principle this term can still be introduced phenomenologically, this would leave open the question about its dependence on the local environment of a magnetic atom.

The analysis given in the preceding section shows that the presence of the fourth-order term in the Ginzburg–Landau expansion of magnetic energy is related to the heterogeneity of the *shape* of the density of states $D(E)$. Hence, in order to describe the symmetry-breaking magnetic phase transition it is necessary to extend the treatment based on equations (9)–(11) beyond the rectangular band model.

In the spirit of the Finnis definition [14] of the quality parameter of a model as the ratio of its predictive power to its complexity, we look for the simplest model of the density of states exhibiting a magnetic phase transition and investigate the generalized parabolic band case, which we then link to the treatment of magnetism based on equations (9)–(11) and the Ginzburg–Landau model. By following this approach, we derive an approximate expression for the embedding function of the magnetic many-body potential model, and study its behaviour over a range of effective electron densities. We then investigate how well the model fits the equilibrium parameters of α-iron, as well as the energies and structures of several fundamental point defect configurations. We find that in order to formulate a working scheme suitable for molecular dynamics simulations it is necessary to ensure that not only the effective embedding functional itself, but also its first *and* its second derivatives are adjusted appropriately in a way consistent with experimental and *ab initio* data.

We assume that the density of states $D(E)$ has a scalable form

$$D(E) = \frac{1}{W} F\left(\frac{E}{W}\right), \tag{23}$$

where W is a scaling parameter that has the meaning of the width of the d band. Function (23) is normalized by the condition

$$2\int_{-\infty}^{\infty} {\rm d}E\, D(E) = \mathcal{N}, \tag{24}$$

where $\mathcal{N} = 10$ is the total number of d orbitals per atom. It is evident that the value of integral (24) is independent of the width of the band W. To show this we introduce a dimensionless variable of integration $X = E/W$ and write

$$2\int_{-\infty}^{\infty} {\rm d}E\, D(E) = 2\int_{-\infty}^{\infty} \frac{{\rm d}E}{W} F\left(\frac{E}{W}\right) = 2\int_{-\infty}^{\infty} {\rm d}X\, F(X) = \text{constant}. \tag{25}$$

In a non-magnetic state the probabilities of populating the spin-up and spin-down states are the same. If we choose the origin of the energy axis at the Fermi energy of the non-magnetic state we find that the total number of electrons occupying the band equals

$$N = 2\int_{-\infty}^{0} {\rm d}E\, D(E). \tag{26}$$

Applying the scaling argument (23) to equation (26) we see that the number of electrons per atom N remains independent of W, as required by the local charge neutrality condition [27, 28].

We now assume that near the origin (or, equivalently, in the vicinity of the Fermi energy of the non-magnetic state) the density of states $D(E)$ is approximated by a sum

$$D(E) = \frac{1}{W}F\left(\frac{E}{W}\right) = \frac{1}{W}\left[a - b\left(\frac{E}{W}\right)^2\right] + \frac{1}{W}R\left(\frac{E}{W}\right), \tag{27}$$

of a parabolic term and a regular part, where $a > 0$ and $b > 0$ are constant factors independent of W, and $|R(0)| \ll a$. The function $R(E/W)$ in equation (27) is chosen in such a way that the representation (27) is *exact*. Formula (27) is valid within the interval of energies where $|E| < W\sqrt{a/b}$.

Consider now a symmetry-broken magnetic state where the populations of spin-up and spin-down states are no longer equal. Since the parabolic term in (27) gives the leading contribution to the density of states near the Fermi energy of the non-magnetic state, in the ferromagnetic state the Fermi energies of spin-up and spin-down states are shifted symmetrically up and down the energy axis $\epsilon_{F\uparrow} = \Delta$ and $\epsilon_{F\downarrow} = -\Delta$. Using equations (26) and (27) we find that

$$\begin{aligned} N_\uparrow &= \int_{-\infty}^{\epsilon_{F\uparrow}} \frac{\mathrm{d}E}{W}F\left(\frac{E}{W}\right) \approx \frac{N}{2} + \int_0^{\Delta} \frac{\mathrm{d}E}{W}\left[a - b\left(\frac{E}{W}\right)^2\right] = \frac{N}{2} + a\left(\frac{\Delta}{W}\right) - \frac{b}{3}\left(\frac{\Delta}{W}\right)^3, \\ N_\downarrow &= \int_{-\infty}^{\epsilon_{F\downarrow}} \frac{\mathrm{d}E}{W}F\left(\frac{E}{W}\right) \approx \frac{N}{2} + \int_0^{-\Delta} \frac{\mathrm{d}E}{W}\left[a - b\left(\frac{E}{W}\right)^2\right] = \frac{N}{2} - a\left(\frac{\Delta}{W}\right) + \frac{b}{3}\left(\frac{\Delta}{W}\right)^3. \end{aligned} \tag{28}$$

These equations show that

$$\begin{aligned} N &= N_\uparrow + N_\downarrow = \text{constant}, \\ \zeta &= N_\uparrow - N_\downarrow = 2\left(\frac{\Delta}{W}\right)\left[a - \frac{b}{3}\left(\frac{\Delta}{W}\right)^2\right]. \end{aligned} \tag{29}$$

Similarly, we find the band part of the total energy

$$\begin{aligned} E_{\text{band}} &\approx \int_{-\infty}^{0} \frac{\mathrm{d}E}{W}EF\left(\frac{E}{W}\right) + \int_0^{\Delta} \frac{\mathrm{d}E}{W}E\left[a - b\left(\frac{E}{W}\right)^2\right] + \int_0^{-\Delta} \frac{\mathrm{d}E}{W}E\left[a - b\left(\frac{E}{W}\right)^2\right] \\ &= -\text{constant} \cdot W + aW\left(\frac{\Delta}{W}\right)^2 - \frac{b}{2}W\left(\frac{\Delta}{W}\right)^4, \end{aligned} \tag{30}$$

where the constant factor in the first term is positive and arises from contributions from both the parabolic and the regular part of $D(E)$. To take into account the electron correlation effects responsible for the ferromagnetic instability we add the Stoner term to (30) and arrive at

$$E_{\text{tot}} = -\text{constant} \cdot W + a\left(\frac{\Delta}{W}\right)^2 (W - Ia) + \frac{b}{2}\left(\frac{\Delta}{W}\right)^4 \left(\frac{4}{3}Ia - W\right) + \cdots. \tag{31}$$

We note that everywhere in the region of the Stoner instability, where $I > W/a$, the fourth-order term in equation (31) is positive and hence (31) agrees with the phenomenological Ginzburg–Landau model (21). The fact that the variable in expansion (31) is not the magnetic moment ζ but the Fermi energy shift Δ is of no significance here since, according to equation (29), Δ is a unique function of ζ. The minimization of function $E_{\text{tot}}(\Delta)$ is therefore equivalent to the minimization of $E_{\text{tot}}(\zeta)$.

Application of the Stoner criterion of magnetic instability to the parabolic band model (31) gives $I > W/a$. If the Stoner criterion is satisfied then the fourth-order term in (31) is

positive and $E_{\rm tot}$, treated as a function of Δ, has the double-well structure shown in figure 2. Function (31) is minimum at the point

$$\left(\frac{\Delta}{W}\right)^2 = \frac{a}{b}\frac{(Ia - W)}{(\frac{4Ia}{3} - W)}, \tag{32}$$

where the total energy is equal to

$$E_{\rm tot}|_{\rm min} = -\text{constant} \cdot W - \frac{a^2}{2b}\frac{(Ia - W)^2}{(\frac{4Ia}{3} - W)}\Theta(Ia - W). \tag{33}$$

Here $\Theta(x)$ is the Heaviside function, $\Theta(x) = 1$ for $x > 0$ and $\Theta(x) = 0$ for $x < 0$.

Formula (33) shows that spontaneous symmetry breaking driven by the Stoner magnetic instability occurring for $I > W/a$ reduces the energy of the system by the amount given by the second term in (33). The stable magnetic configuration has lower energy than the (unstable) non-magnetic state, the energy of which is given by the first term in (33). Due to the presence of the Heaviside function in equation (33) the magnetic part of the total energy vanishes in the limit where the band width W is large, i.e. in the limit where the material is compressed.

Using equation (33) and following the argument based on the Finnis–Sinclair model [13, 14], where the bandwidth W is assumed to be proportional to an effective pairwise density function ρ, we arrive at an empirical embedding functional describing *both* the magnetic and the non-magnetic states of the material,

$$F[\rho] = -A\sqrt{\rho} - B\frac{\left(\sqrt{\rho_{\rm c}} - \sqrt{\rho}\right)^2}{\left(\upsilon + \sqrt{\rho_{\rm c}} - \sqrt{\rho}\right)}\Theta\left(\rho_{\rm c} - \rho\right). \tag{34}$$

Here A and B are constant factors, $\rho_{\rm c}$ is a critical value of effective density at which magnetism vanishes, and υ is a small positive constant. In what follows we investigate and improve this functional, and apply it to model strongly distorted atomic configurations in the vicinity of interstitial defects in α-iron.

Summarizing the results of this section, we see that effects of ferromagnetism can be described by adding a new term to the potential of a system of non-magnetic interacting atoms. This conclusion comes naturally from the treatment based on the Ginzburg–Landau model where the energy of a symmetry-broken configuration is lower than the energy of a higher-symmetry configuration *used as a reference*. In our case the reference non-magnetic configuration is described by the Finnis–Sinclair potential model, and the second term in (34) is the energy gained due to the formation of a symmetry-broken ferromagnetic configuration.

4. Parametrization and numerical examples

The embedding functional (34) is a sum of two terms. The first term is proportional to the square root of the effective pairwise density function, ρ, and is therefore conceptually equivalent to the embedding functional of the Finnis–Sinclair model [13]. The second term describes effects of magnetism, and it vanishes *quadratically* as the density ρ approaches the critical value $\rho_{\rm c}$. It is significant that both the embedding functional *and* its first derivative are continuous at the critical point $\rho = \rho_{\rm c}$, since functional (34) describes a second-order phase transition where the energy and all of its first derivatives have to remain continuous [30] at the point of transition.

The dependence of functional $F[\rho]$ on density is illustrated in figure 3. For large values of $\rho_{\rm c} - \rho \gg \upsilon$ the functional is linear in $\rho_{\rm c} - \rho$, namely

$$F[\rho] \approx -A\sqrt{\rho} - B\left(\sqrt{\rho_{\rm c}} - \sqrt{\rho}\right)\Theta\left(\rho_{\rm c} - \rho\right). \tag{35}$$

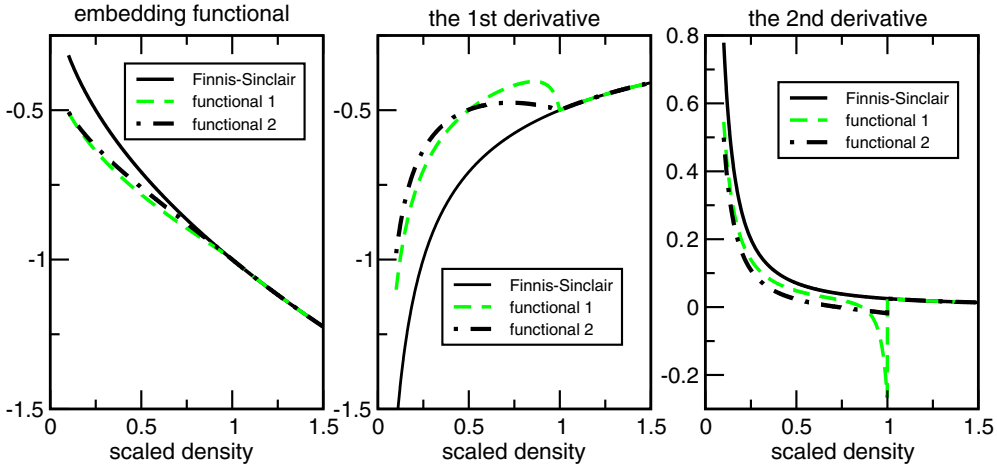

Figure 3. This figure shows the two effective embedding functionals (34) (functional 1) and (37) (functional 2), as well as their first and second derivatives, plotted as functions of the scaled density ρ/ρ_c. Note the strong discontinuity of the second derivative of functional 2 at the magnetic phase transition point $\rho/\rho_c = 1$. Curves shown in this figure were calculated assuming that $B = 0.3$ and $\upsilon = 0.05$.

For small values of $\rho_c - \rho \ll \upsilon$ it is of the second order in $\rho - \rho_c$, in agreement with the Ginzburg–Landau approximation (22),

$$F[\rho] \approx -A\sqrt{\rho} - \frac{B}{\upsilon}\left(\sqrt{\rho_c} - \sqrt{\rho}\right)^2 \Theta\left(\rho_c - \rho\right). \tag{36}$$

While the functional behaviour of $F[\rho]$ in the two limiting cases (35) and (36) is qualitatively correct, the second derivative of (34) has a cusp near the point $\rho \approx \rho_c$. This cusp is visible in figure 3, and it is due to the small value of υ in the denominator of (34). To improve the behaviour of the second derivative while retaining the general properties of the $F[\rho]$ and its first derivative at $\rho \approx \rho_c$ we replace (34) with

$$F[\rho] = -A\sqrt{\rho} - \frac{B}{\ln 2}\left(1 - \sqrt{\frac{\rho}{\rho_c}}\right)\ln\left(2 - \frac{\rho}{\rho_c}\right)\Theta\left(\rho_c - \rho\right). \tag{37}$$

This functional and its first derivative are continuous at $\rho = \rho_c$ while the second derivative of (37) no longer has a cusp near the critical point. Figure 3 illustrates the difference in the behaviour of derivatives of functionals (34) and (37) as functions of the effective density ρ. Functional (37), as well as equation (33), both have an important property that we expect from a magnetic embedding functional, namely, the occurrence of a symmetry breaking phase transition at $\rho = \rho_c$. In the high density limit $\rho > \rho_c$ only the non-magnetic solution is stable, while in the low density limit $\rho < \rho_c$ the functional splits into two branches, a magnetic one given by (37) and a non-magnetic one given by the same formula (37) where $B = 0$. The numerical study described below is based on the functional form of the embedding term given by (37).

With (37) we now have a physically justifiable description for the magnetic band energy and, with the addition of a pairwise repulsive potential term, $V(r)$, a fully empirical model that can be used to perform molecular dynamics of a multi-million atom configuration with the same efficiency as that of previous non-magnetic empirical models for iron. The total energy

of such an N-atom system is given by

$$E_{\rm tot} = \sum_{i}^{N} F[\rho_i] + \tfrac{1}{2} \sum_{ij, i\neq j}^{N} V(r_{ij}), \tag{38}$$

where

$$\rho_i = \rho_{\rm c} \sum_{j, i\neq j} f(r_{ij}). \tag{39}$$

Here $f(r)$ is the so-called pairwise density radial function that, in the context of the second-moment description [14], represents the magnitude squared of the (two-centre) hopping integral between atoms separated by a distance r. Thus, through appropriate forms of $f(r)$ and $V(r)$, and values of A and B in (37), the inter-atomic model becomes fully defined.

Via the embedded atom method (EAM) [31], $\rho_{\rm c} f(r_{ij})$ may be viewed as the electronic density at i due to atom j, where $F[\rho_i]$ is termed the embedding energy of atom i. Unlike the square root band term in the second moment representation, the functional form of the embedding function within the EAM formalism is a free parameter of the model and moreover cannot be uniquely defined since the total energy is invariant with respect to the transformation:

$$F[\rho_i] \rightarrow F[\rho_i] + \kappa\rho_i \tag{40}$$

$$V(r_{ij}) \rightarrow V(r_{ij}) - 2\kappa\rho_{\rm c} f(r_{ij}). \tag{41}$$

Here κ is a constant that determines the first derivative of the embedding energy at (say) the equilibrium lattice constant. The present magnetic model assumes a multi-valued band energy term *but not* a multi-valued pairwise repulsive term, and hence the inherent arbitrariness of the embedding energy functional within the EAM formalism is not present since the transformation contained in equations (40) and (41) would effectively introduce a non-physical multi-valued repulsive potential term.

Two important features of the functional forms are that $f(r)$ must always be positive, and both $f(r)$ and $V(r)$ must be relatively short range. Indeed, efficient electronic screening and effective renormalization of the relevant hopping integrals dictate that the repulsive potential and pairwise density radial functions should not extend far beyond the bcc second nearest neighbour and fcc first nearest neighbour shells. With these issues in mind we choose a summation of cubic knot functions to represent both $f(r)$ and $V(r)$:

$$f(r) = \sum_{n=1}^{N^f} f_n (r - r_n^f)^3 \Theta(r - r_n^f) \tag{42}$$

$$V(r) = \sum_{n=1}^{N^V} V_n (r - r_n^V)^3 \Theta(r - r_n^V), \tag{43}$$

where the knot coefficients f_n and V_n, and the knot points r_n^f and r_n^V are to be determined. This functional form has the advantage of being flexible with no initial assumption of overall shape, being continuous up to the second derivative, and already having a smooth cut-off with the introduction of the first knot function. Moreover, additional shorter range knot functions can be added without affecting the functional form at larger radial distances. Such a representation has been used in previous non-magnetic empirical models of iron [15, 16].

For the present work, the database of material properties used to obtain a physically viable fit consists of the bulk cohesive energy, lattice constant and combinations of the elastic stiffness constants of both the bcc and fcc, magnetic and non-magnetic, phases. In addition, the un-relaxed vacancy formation energy and relaxed $\langle 100\rangle$, $\langle 110\rangle$ and $\langle 111\rangle$ interstitial dumbbell energies are included. The interstitial energies are obtained by relaxing geometrically

Table 1. Converged values of bulk properties of magnetic and non-magnetic fcc and bcc structures for case studies I and II and in parenthesis the corresponding database values. For the 'pressure' row, the converged pressure for the lattice constant shown in parenthesis is given. For the 'cohesive energy' row the higher energy phases are given relative to the bcc equilibrium cohesive energy. Converged values shown in italics were not included in the objective function.

	FM bcc[a]	NM bcc[b]	FM fcc[b]	NM fcc[b]
		Case study I		
E_0 (eV)	−4.3160 (−4.3160)	0.4457 (0.4762)	0.1863 (0.1361)	0.4742 (0.1565)
Pressure (GPa) (l_0 (Å))	0.0 (2.866)	−0.0324 (2.7727)	0.0426 (3.4934)	−0.0732 (3.4608)
B (GPa)	173.1 (173.1)	227.5 (276)	112.3 (182)	192.4 (317)
C_{44} (GPa)	121.9 (121.9)	*188.4* (141)	*154.2* (23)	*186.5* (287)
C' (GPa)	52.5 (52.5)	*−33.7* (−110)	*−83.5* (−77)	*−48.4030* (125)
		Case study II		
E_0 (eV)	−4.3160 (−4.3160)	0.1930 (0.4762)	0.1355 (0.1361)	0.2216 (0.1565)
Pressure (GPa) (l_0 (Å))	0.0 (2.866)	−0.0143 (2.7727)	0.0426 (3.4934)	0.0529 (3.4608)
B (GPa)	173.1 (173.1)	249.2 (276)	197.8 (182)	305.4 (317)
C_{44} (GPa)	121.9 (121.9)	*172.1* (141)	*151.6* (23)	*179.9* (287)
C' (GPa)	52.5 (52.5)	*−21.0* (−110)	*56.2*(−77)	*49.3223* (125)

[a] Database values taken from [15].
[b] Database cohesive energy and lattice constant taken from figure 2 of [6], and elastic stiffness constants taken from [32].

Table 2. Unrelaxed vacancy and relaxed interstitial energies produced by *ab initio* calculations and converged values for case studies I and II. In the case of the vacancy energy, the values within parenthesis are for the relaxed structures. Model values in italics were not included in the objective function.

	Ab initio[a]	Case study I	Case study II
E_{vac} (eV)	−(2.07)	2.25 (2.18)	2.07 (1.97)
$E_{\langle 100\rangle}$ (eV)	4.64	*4.28*	4.60
$E_{\langle 111\rangle}$ (eV)	4.34	*4.01*	4.24
$E_{\langle 110\rangle}$ (eV)	3.64	*4.11*	3.65

[a] Reference [11]. In the present work the relaxed *ab initio* value was taken as the database value for the un-relaxed vacancy formation energy.

constructed dumbbell configurations using a conjugate-gradient procedure. In practice, 433-atom interstitial configurations were used rather than the 129-atom systems of Fu *et al* [11] from which the database interstitial energies are taken. Such relaxations must be performed for each candidate parameter set. Finally, the bcc/fcc transition point in terms of volume per atom is included. Inspection of the *ab initio* [6] and tight-binding [7] equation-of-state (EOS) curves reveal that in the region where the magnetic fcc phase becomes more stable there is a significant reduction of the fcc magnetic moment reflecting an increase in the local density and a corresponding 'switching off' of the magnetic interaction. This feature was also included in the materials database by adding a term in the objective function that approached zero if the fcc local electronic density approached the critical density at the bcc/fcc transition point.

Tables 1 and 2 list the numerical values for the material properties and their corresponding sources. We note that many of the physical quantities in these tables are obtained from a number of different *ab initio* calculations of varying accuracy and that the energies, lattice constants and elastic stiffness constants of the higher energy phases enter the final objective function only with minimal weights. In the actual fitting a complex and changing choice of weights was used to obtain optimal parameter sets, with the associated strategy developed by

real-time computational steering of the fitting procedure to gain insight into the non-linear behaviour of the changing objective function.

If the objective function contains data derived from the relaxation of the interstitial configurations, derivative information is not available with respect to all of the fitting parameters and therefore a combination of simulated annealing [33] and a non-linear downhill simplex algorithm [34], both of which do not employ derivative information, are used to minimize the objective function. Both of these techniques are controlled by a master algorithm that can (1) reject outright a candidate solution and (2) identify a local minimum and an associated exit path. The first property was found to be more efficient than adding additional penalty terms to the objective function, and the second property was found to be absolutely essential for the computationally intensive task of finding the necessary optimal solution in a objective function landscape rich in local minima. In addition to the above procedures, the embedding energy coefficients (A and B) and the outermost three knot coefficients of the repulsive potential could be solved for exactly through a linear matrix solution to correctly reproduce the bcc magnetic cohesive energy, lattice constant and elastic stiffness constants. Thus the numerical part of the fitting procedure involved searching for the optimal knot coefficients f_n (for all n) and V_n (for $n > 3$). The knot points are chosen initially and kept constant throughout the optimization.

In what follows we consider two case study fits that demonstrate the power of the current empirical magnetic model. In case study I we present a fit that only includes the bulk bcc and fcc properties and the unrelaxed vacancy formation energy, whilst in case study II we present a fit that is optimized to reproduce the correct relaxed interstitial energies to an accuracy of less than 0.1 eV. In both fits a minimal number of knot functions are used: six for the pairwise repulsive potential and only four for the pairwise density term. In case study II, two additional short range knot functions are used in both radial functions to refine the interstitial energies. Whilst not always producing the smallest value of the objective function, such a minimal choice will ensure optimal smoothness in the radial functions.

4.1. Case study I

In case study I, the bulk magnetic bcc properties (cohesive energy, lattice constant and elastic stiffness constants), the vacancy formation energy and the *isotropic* bulk properties (cohesive energy, lattice constant and bulk modulus) of the non-magnetic bcc phase and magnetic and non-magnetic fcc phases are fitted. In particular, the bcc/fcc transition point is included with a significant weight. Table 1 lists the material parameters for the optimal parameter set shown in table 3, and we see that reasonable agreement is obtained for the higher energy phases. This can be better seen in figure 4(a), in which the resulting equation of state (EOS) curves are displayed for the four phases. Comparison of this figure with the *ab initio* EOS curves of Herper *et al* [6] demonstrates that apart from the non-magnetic fcc phase, good qualitative agreement exists with the magnetic bcc/fcc transition point being well reproduced—although ρ_{fcc} approaching ρ_{c} in the fcc/bcc transition region could not be achieved, reflecting the too high non-magnetic fcc EOS curve. Despite the non-magnetic fcc EOS curve being too high, the magnetic energy contribution to the magnetic fcc cohesive energy remains smaller than in the bcc case. Thus the model displays the important physical property that the magnetic fcc structure has a higher energy than the corresponding bcc structure because the magnetic contribution to the energy of the former is less. This is further reflected in figure 4(b), which displays the resulting bcc and fcc local electronic densities as a function of volume per atom, where we see that the bcc local electronic density is less than the corresponding fcc value. The origin of the correct ordering of the local electronic density can be seen in figure 4(c), where the pairwise density radial function is shown. As expected, it is short range, with the

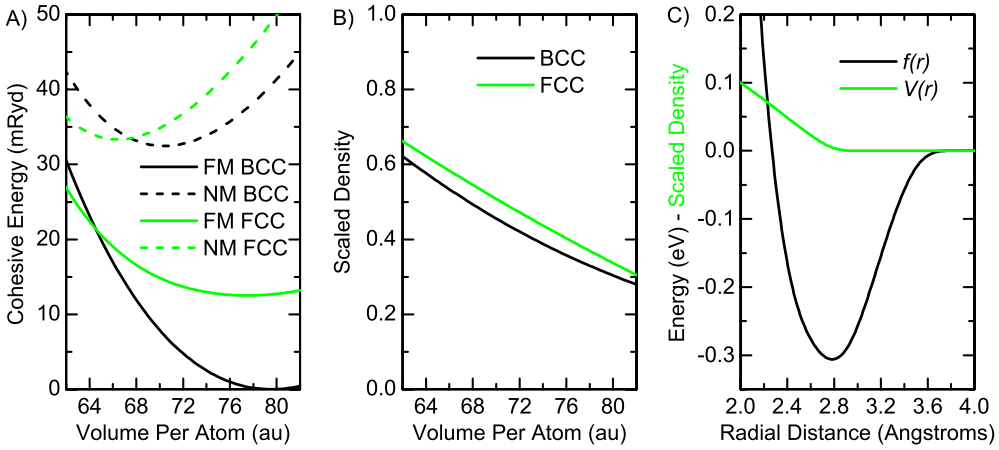

Figure 4. Plot of (a) equation of state curves, (b) scaled local electronic density and (c) pairwise density and repulsive potential radial functions of case study I.

Table 3. Optimal parameter set for case studies I and II.

	Case study I	Case study II
A	3.527 586 256 672 234	4.100 199 340 884 814
B	1.642 855 167 616 477	1.565 647 547 483 517
r_n^f	f_n	
3.0	0.505 568 175 375 7052	0.933 205 668 108 8162
$2.8\dot{6}$	−0.425 555 283 113 6833	−1.162 558 782 567 700
$2.7\dot{3}$	−0.562 940 810 933 9820	−0.350 202 694 924 9225
2.6	0.431 853 088 566 5762	0.428 782 083 543 0028
2.4	—	4.907 925 057 809 273
2.3	—	−5.307 049 068 415 304
r_n^f	V_n	
4.1	$1.753\,386\,111\,560\,4772 \times 10^{-3}$	−0.196 067 438 741 9232
3.8	−0.932 121 957 205 9338	0.368 752 593 542 2963
3.5	1.696 463 955 030 590	−1.505 333 614 924 853
3.2	0.663 847 872 510 9788	4.948 907 078 156 191
2.9	−1.914 559 267 568 704	−4.894 613 262 753 399
2.6	3.193 687 184 255 540	3.468 897 724 782 442
2.4	—	−1.792 218 099 820 337
2.3	—	80.220 695 922 469 87

dominant contribution for the bcc structure being at the bcc first nearest neighbour distance, with the radial function dropping to ∼96% at the second nearest neighbour distance. Thus the bcc electronic density is constructed mainly from its eight first nearest neighbours, giving a density value that is less than that obtained from the 12 more distant first nearest neighbours of the fcc structure.

Table 2 lists the optimized un-relaxed vacancy formation energy and the predicted constant volume relaxation energy calculated by relaxing a 431-atom single-vacancy configuration at fixed bulk equilibrium volume, along with an *ab initio* value derived from a $54-1$ atom cell that did involve volume relaxation. We note that there exists a spread of *ab initio* derived relaxed

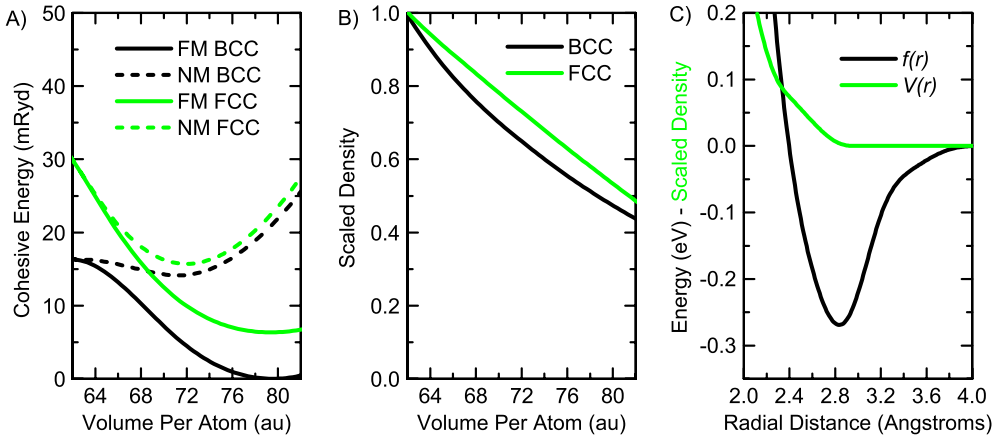

Figure 5. Plot of (a) equation of state curves, (b) scaled local electronic density and (c) pairwise density and repulsive potential radial functions of case study II.

vacancy formation energies and the accepted experimental value is 2 ± 0.2 eV (see [11] and references therein). Figure 6(a) displays the predicted vacancy migration barrier calculated by relaxing all forces normal to the reaction coordinate path as a function of the migrating atom's position. A plateau structure is evident at a barrier height of approximately 0.85 eV. Such a feature is also seen in a recent *ab initio* calculation [12]; however, in previous non-magnetic empirical models a double-bump structure is produced [16]. The barrier height itself is similar in value to that of the non-magnetic empirical model of Ackland *et al* [15] and 0.18 eV higher than that derived from *ab initio* [11].

Table 2 also lists the *predicted* interstitial energies and we see that the energy range is of the correct order of magnitude, but the ordering is incorrect. Refining the fit, by including the interstitial energies in the objective function without compromising the EOS curves in figure 4(a), improved somewhat the situation, with the $\langle 100 \rangle$ energy approaching the *ab initio* database value. However, the correct ordering of the $\langle 110 \rangle$ and $\langle 111 \rangle$ energies could not be achieved, where at best the $\langle 110 \rangle$ and $\langle 111 \rangle$ energies became nearly degenerate. The addition of two more knot functions at 2.4 and 2.3 Å to both $f(r)$ and $V(r)$ did not help.

4.2. Case study II

In case study II the bulk equilibrium properties, vacancy formation energy and interstitial energies were fitted. As in case study I the isotropic bulk equilibrium properties of the non-magnetic bcc phase, and the magnetic and non-magnetic phases were also included in the objective function. The initial stage of this fit used the same knot function representation as in case study I and involved increasing (during the fitting) the weights for the interstitials. This implicitly compromised the magnetic bcc/fcc transition point but resulted in the correct ordering of the interstitial energies. To achieve the required accuracy of less than 0.1 eV two inner knot functions were added to both the pairwise density and repulsive potential functions. Tables 1 and 2 display the physical properties of the optimal parameter set, which is shown in table 3.

Figure 5(a) displays the resulting EOS curves and we see that the bcc/fcc transition point is not at all reproduced; indeed, the energies as functions of high compression differ greatly from that of case study I and the predictions of the *ab initio* EOS curves. Despite this, once

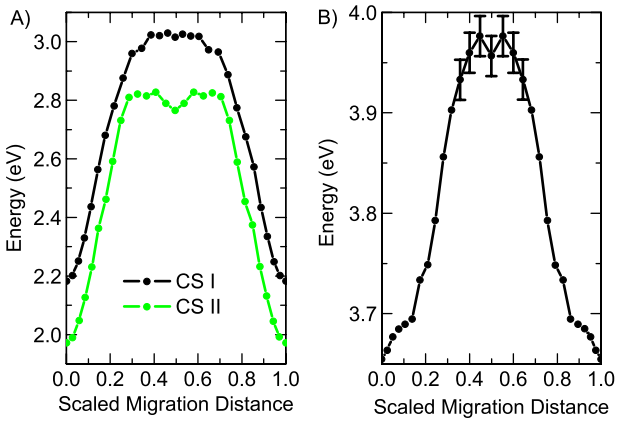

Figure 6. (a) Vacancy migration energy curves for case studies I and II. (b) ⟨110⟩ self-interstitial migration energy curve for case study II.

again the magnetic energy contribution of the fcc structure is less than that of the bcc structure. Moreover, in figure 5(b) we see that the bcc density has the required (equilibrium) property that it is less than the corresponding fcc electronic density. Figure 5(c) displays the pairwise density and repulsive potential radial functions and we see that both are smooth functions of distance, containing no additional anomalous non-monotonic structure. Inspection of the pairwise density radial function shows that it has a similar form to that of case study I for equilibrium bcc and fcc lattice inter-atomic distances, with a change in slope at distances less than 2.4 Å due to the additional inner knot functions. The pairwise repulsive potential is also quantitatively similar to that of case study I; however, it is somewhat more extended at the larger inter-atomic distance range and, although not evident in the graph, the region at less than 2.4 Å differs greatly (see knot coefficients in table 3).

The predicted constant volume vacancy relaxation energy is listed in table 2 and found to be similar to that of case study I; however, inspection of the associated migration energy curve (see figure 6(a)) now reveals a double-bump structure and not the plateau structure seen in case study I. The corresponding migration barrier height of 0.84 eV is similar to that of case study I. Despite the difference in the barrier region structure, case studies I and II do give the same vacancy energy characteristics, reflecting that both fits exhibit similar equilibrium bulk bcc properties.

Figure 6(b) displays the migration energy path of the ⟨110⟩ interstitial defect calculated using the nudged-elastic-band method [35], and we see that the barrier region exhibits a double-bump structure. Investigation of this region however reveals alternative minimum energy paths, some of which exhibit a plateau or single-bump structure—with all having very similar maximum migration energies. These alternative paths can be found by varying the spring constants and also the number of replica points within the nudged-elastic-band procedure, indicating a rich and non-trivial energy landscape, albeit at an energy scale of ∼0.01 eV. We therefore leave it as an open question (through the inclusion of error bars in figure 6(b)) whether or not the true minimum energy path is a single-bump barrier for the present potential as was found in the case of *ab initio* calculations [12]. The corresponding barrier height is 0.32 eV, which is in excellent agreement with the *ab initio* result [12] of 0.34 eV. Investigation of the associated reaction coordinate path indicates that the migrating ⟨110⟩ dumbbell executes a roughly rotational motion around a [111] direction to avoid the higher energy ⟨111⟩ configuration.

5. Discussion

An important difference between the presented case studies is that in case study II the local electronic densities are larger in value and therefore approach more rapidly the critical scaled density ($\rho_c = 1$) at which magnetism is turned off. Indeed, this is the origin of why case study II has lower energy EOS curves for the non-magnetic phases when compared to those of case study I. In case study I the typical electronic densities are at values for which the magnetic embedding energy exhibits linear behaviour, whereas in case study II the electronic density values are in the range where the embedding energy can become more quadratic-like (especially close to $\rho = \rho_c$), giving the fit the ability to reduce the magnetic contribution to the energy more rapidly as a function of increasing electronic density. It is for this reason that case study II can correctly reproduce the dumbbell interstitial energies, correlating well to the *ab initio* [10] and tight binding [7] result, that at and around the interstitial there is a reduction in the magnetic moment and thus a reduction in the contribution of magnetism to the defect energies.

That the magnetic contribution plays a vital role in obtaining the correct interstitial energies can be further illustrated by inspection of the *ab initio non-magnetic* interstitial energies derived from the converged (magnetic) interstitial positions of Fu *et al* [11]. Using the (128 + 1)-atom $\langle 100 \rangle$, $\langle 111 \rangle$ and $\langle 110 \rangle$ configurations these are 2.29, 0.91 and 1.01 eV respectively, and for the (54 + 1)-atom $\langle 111 \rangle$ and $\langle 110 \rangle$ configurations these are 1.47 and 1.08 eV respectively[4]. Although there is a variance in these preliminary *ab initio* results, we see that a significant part of the total energy of each of the defects arises from magnetism. In fact, across the three interstitial energies there are significant differences in the magnetic contribution, which is in agreement with the trend of the magnetic moment signatures [7, 10], and is also responsible for the anomalous ordering in iron of the $\langle 111 \rangle$ and $\langle 110 \rangle$ interstitial energies when compared to other group VI materials. Case study II predicts non-magnetic interstitial energies of 2.05, 1.63 and 1.21 eV, which are qualitatively similar to the *ab initio* results in terms of range and difference—a remarkable result given that only the trend of the non-magnetic bcc elastic constants is reproduced (see table 1). On the other hand, case study I gives as its non-magnetic interstitial energies 2.17, 1.86 and 1.95 eV, the spread of which is much smaller, reflecting the lower local electronic density values contained in figure 4(b).

The presented case studies reveal that the correct ordering of the interstitial energies could only be achieved through the appropriate magnetic contribution to the bulk cohesive energy and its associated volume dependence, and that the use of short range knot functions could only help in the fine tuning of the final defect energies. Thus the region surrounding the interstitial core, loosely defined as the two atoms constituting the original geometrical dumbbell, plays a vital role in these energies. *Ab initio* [10] and tight-binding [7] calculations reflect this in distinctly different perturbed moment fields around the cores of the three interstitials demonstrating the importance of the linear and non-linear magneto-elastic field energy contribution. Such moment fields can be investigated within the present empirical model since each atom carries with it a moment that is determined by some function of $1 - \sqrt{\rho/\rho_c}$, where ρ is the atom's local electronic density. The form of this function will not be considered in the present work. We note however that the ability of the present empirical model to predict moment distributions of interstitials, more complex defect structures such as extended dislocation structures, as well as artificially grown magnetic nanostructures consisting of millions of atoms, opens up a new and exciting direction for the empirical modelling of α-iron and iron-based magnetic alloys.

[4] For the (128 + 1)-atom non-magnetic calculation, VASP V4.6 was used with a $2 \times 2 \times 2k$-point mesh; see Nguyen-Manh [36]. For the (54 + 1)-atom case, SIESTA was used with a $3 \times 3 \times 3k$-point mesh, see Fu and Willaime [36].

That the bcc/fcc transition point cannot be reproduced, even qualitatively, whilst at the same time maintaining the correct interstitial ordering is not surprising since the fcc electronic DOS differs in shape from the bcc electronic DOS shown in figure 1—a feature that a second moment description of the DOS cannot achieve if the physically justified short range nature of the radial functions is to be retained. Case study I achieves this somewhat fortuitously and is probably a result of the added flexibility of the magnetic energy functional. Such structural energetics can (and should be) achieved by going to a higher moment description of the DOS that allows the modelling of the environmental dependence of the bi-modal and/or asymmetric aspects of the DOS. Moreover, the inability of the present second moment description to capture the differences between the bcc and fcc DOSs is also seen in the model's inability to capture the related fcc properties of a significantly more rapid moment reduction as a function of compression (see figure 2 in [6]) and a much smaller magnetic energy contribution to the bulk cohesive energy. This can be understood in terms of the Ginzburg–Landau description contained in figure 2 and (21), since both α and β will also depend on the general shape of the fcc DOS.

Finally, we remind the reader that the present optimal fit (case study II) contained in table 3 is not suitable for primary damage state cascade evolution simulation. Following the approach of [15], the appendix includes the high energy (short range) corrections necessary to begin performing such simulations. As with all previous empirical potentials that employ such a short range correction, this type of modification may not correctly describe, in a quantitative sense, the intermediate threshold kinetic energy regime (the minimum kinetic energy need to displace an atom). More generally we caution the reader that the current fit is in its infancy and will no doubt undergo future development through validation and further refinement via the expansion of the physical database contained within tables 1 and 2.

6. Concluding remarks

Although the fine details of the electronic density of states as a function of spin resolved Fermi energies do play an important role in determining the magnetic properties of α-iron, the present work demonstrates that in terms of the equilibrium magnetic moment, the magnetic energy contribution to the band energy can be well represented by a Ginzburg–Landau mean field theoretic model. This result considerably simplifies the problem of modeling the environmental dependence of the magnetic energy, avoiding the need to accurately model the electronic density of states and allowing only a second moment description of the electronic density of states through the parabolic functional form to suffice.

Acknowledgments

We are grateful to David Pettifor, Adrian Sutton, Tony Paxton and Ralf Drautz for stimulating discussions, and to Graeme Ackland for making a preprint of his paper [17] available to us before publication. We would like to acknowledge a comment by Professor L M Brown, who confirmed our thoughts about the occurrence of a magnetic phase transition in the core of an edge dislocation in α-iron. We would like to thank Duc Nguyen Manh for the provision of the tight-binding density of states of bcc iron and for performing trial density functional calculations of formation energies of defects in the non-magnetic iron. Coordinates of atoms used as input for these calculations, as well as the unpublished values of energies of formation of self-interstitial atoms defects in the non-magnetic iron, were kindly made available to us by Chu-Chun Fu and François Willaime. Finally, we would like to thank Max Victoria for

bringing the question about magnetic interactions in iron to our attention and for his continuing interest in this problem.

Work at the UKAEA Culham Science Centre was supported by the UK Engineering and Physical Sciences Research Council (EPSRC), by EURATOM and by the PERFECT Integrated Project under contract number F16O-CT-2003-508840. This work was also supported by a travel grant provided to one of the authors (PMD) by the EURATOM staff mobility programme.

Appendix. Repulsive potential modification for radiation damage simulations

For primary damage state simulation, the short range properties of the interatomic model need to be modified to correctly describe the high energy collision dynamics of the early stages of cascade evolution. This is generally done by modifying the repulsive pair potential so that at some short range distance the potential converges to the universal screened Coulomb potential of Biersack and Ziegler [37]:

$$V_{bz}(r) = \frac{Z^2 e^2}{4\pi\varepsilon_0 r}\phi\left(\frac{r}{a_s}\right), \tag{A.1}$$

where the screening function is

$$\phi(x) = 0.1818\exp(-3.2x) + 0.5099\exp(-0.9423x) + 0.2802\exp(-0.4029x) + 0.02817\exp(-0.2016x) \tag{A.2}$$

and the screening length is

$$a_s = \frac{0.885\,34 a_B}{\sqrt{2}Z^{\frac{1}{3}}}. \tag{A.3}$$

In the above a_B is the Bohr radius and $e^2/4\pi\varepsilon_0 = 14.3992$ eV Å. The embedding energy remains unchanged, with the assumption that at short distances it contributes negligibly due to the dominance of the above Coulomb term.

Thus the repulsive pair potential will take the following form:

$$V(r) = V_{bz}(r), \qquad r \leqslant r_1 \tag{A.4}$$

$$= V_{it}(r), \qquad r_1 < r < r_2 \tag{A.5}$$

$$= V_{mp}(r), \qquad r \geqslant r_2 \tag{A.6}$$

where $V_{it}(r)$ is an interpolation function and $V_{mp}(r)$ is (43). For the present work the interpolation function is taken as the fifth order polynomial:

$$V_{it}(r) = a_0 + a_1 r + a_2 r^2 + a_3 r^3 + a_4 r^4 + a_5 r^5, \tag{A.7}$$

where the coefficients are chosen to ensure continuity until the second derivative.

In earlier potentials, r_1 was often chosen to be less than or close to 1 Å, and r_2 typically near 2 Å or less. Within this range of interatomic distances, the universal potential has values between 10 and 100 eV, which is the energy regime that controls the threshold displacement energy—the minimum kinetic energy required to displace irreversibly an atom from its lattice position. Thus for many published potentials it is the interpolation function that controls this important regime of interaction, a somewhat unsatisfying situation. For this reason, we choose $r_1 = 1.8$ Å and $r_2 = 2.0$ Å, so that it is the physically based universal potential that dictates the physics of the displacement threshold energy. This choice should be considered as a simple and first approximation to the problem of reproducing the correct bonding physics pertinent to the threshold energy regime. Table A.1 lists the values of the coefficients of (A.7).

Table A.1. Polynomial coefficients for interpolation function (A.7).

n	a_n
0	722 18.368 286 582 99e0
1	−180 889.306 183 357 9e0
2	180 517.151 040 168 7e0
3	−896 48.631 976 308 07
4	221 41.238 736 305 31
5	−2174.252 677 819 831

References

[1] Stoller R E, Zinkle S J, Nichols J A and Corwin W R 2004 *Workshop on Advanced Computational Materials Science: Application to Fusion and Generation IV Fission Reactors, Oak Ridge National Laboratory Report* ORNL/TM-2004/132

[2] Stoneham A M, Matthews J R and Ford I J 2004 *J. Phys.: Condens. Matter* **16** S2597

[3] Hasegawa H and Pettifor D G 1983 *Phys. Rev. Lett.* **50** 130

[4] Bagno P, Jepsen O and Gunnarsson O 1989 *Phys. Rev.* B **40** 1997
Barbiellini B, Moroni E G and Jarlborg T 1990 *J. Phys.: Condens. Matter* **2** 7597
Leung T C, Chan C T and Harmon B N 1991 *Phys. Rev.* B **44** 2923
Singh D J, Pickett W E and Krakauer H 1991 *Phys. Rev.* **43** 11628

[5] Söderlind P, Moriarty J A and Wills J M 1996 *Phys. Rev.* B **53** 14063

[6] Herper H C, Hoffmann E and Entel P 1999 *Phys. Rev.* B **60** 3839

[7] Liu G, Nguyen-Manh D, Liu B-G and Pettifor D G 2005 *Phys. Rev.* B **71** 174115

[8] Dudarev S L, Botton G A, Savrasov S Y, Humphreys C J and Sutton A P 1998 *Phys. Rev.* B **57** 1505
Dudarev S L, Peng L-M, Savrasov S Y and Zuo J M 2000 *Phys. Rev.* B **61** 2506

[9] Ono F, Maeta H and Kittaka T 1984 *J. Phys. Soc. Japan* **53** 920

[10] Domain C and Becquart C S 2001 *Phys. Rev.* B **65** 024103

[11] Fu C-C, Willaime F and Ordejón P 2004 *Phys. Rev. Lett.* **92** 175503

[12] Fu C-C, Dalla Torre J, Willaime F, Bocquet J-L and Barbu A 2005 *Nat. Mater.* **4** 68

[13] Finnis M W and Sinclair J E 1984 *Phil. Mag.* **50** 45

[14] Finnis M W 2003 *Interatomic Forces in Condensed Matter* (Oxford: Oxford University Press) pp 236–7

[15] Ackland G J, Bacon D J, Calder A F and Harry T 1997 *Phil. Mag.* A **75** 713

[16] Mendelev M I, Han S, Srolovitz D J, Ackland G J, Sun D Y and Asta M 2003 *Phil. Mag.* **83** 3977

[17] Ackland G J 2005 *J. Nucl. Mater.* at press; (*Preprint* cond-mat/0505060)

[18] Stoner E C 1939 *Proc. R. Soc.* A **169** 339
Wohlfarth E P 1953 *Rev. Mod. Phys.* **25** 211
Edwards D M and Wohlfarth E P 1968 *Proc. R. Soc.* A **303** 127
Pettifor D G 1980 *J. Magn. Magn. Mater.* **15–18** 847

[19] Kübler J 2000 *Theory of Itinerant Electron Magnetism* (Oxford: Oxford University Press) chapter 4

[20] Landau L D and Lifshitz E M 1977 *Quantum Mechanics. Non-relativistic Theory* 3rd edn (Oxford: Pergamon) pp 223–34

[21] Kadanoff L P *et al* 1967 *Rev. Mod. Phys.* **39** 395

[22] Ziman J M 1972 *Principles of the Theory of Solids* 2nd edn (Cambridge: Cambridge University Press) chapter 10, section 5

[23] Majlis N 2000 *The Quantum Theory of Magnetism* (Singapore: World Scientific) chapter 7, pp 219–23

[24] See Landau L D and Lifshitz E M 1977 *Quantum Mechanics. Non-relativistic Theory* 3rd edn (Oxford: Pergamon) p 253

[25] Imada M, Fujimori A and Tokura Y 1998 *Rev. Mod. Phys.* **70** 1039

[26] Pettifor D G 2003 *Acta Mater.* **51** 5649

[27] Ackland G J, Finnis M W and Vitek V 1988 *J. Phys. F: Met. Phys.* **18** L153

[28] Sutton A P 1993 *Electronic Structure of Materials* (Oxford: Oxford University) pp 174–82

[29] Pettifor D G 1996 *Bonding and Structure of Molecules and Solids* (Oxford: Oxford University Press) pp 223–31
Lomer W M 1961 *Br. J. Appl. Phys.* **12** 535
Gunnarsson O 1976 *J. Phys. F: Met. Phys.* **6** 587

[30] Landau L D and Lifshitz E M 1980 *Statistical Physics* 3rd edn (Oxford: Pergamon) pp 446–56

[31] Daw M S and Baskes M I 1983 *Phys. Rev. Lett.* **50** 1285
Daw M S and Baskes M I 1984 *Phys. Rev.* B **29** 6443
[32] Guo G Y and Wang H H 2000 *Chin. J. Phys.* **38** 949
[33] Corana A, Marchesi M, Martini C and Ridella S 1987 *ACM Trans. Math. Softw.* **13** 262
[34] Nelder J A and Mead R 1965 *Comput. J.* **7** 308
[35] Henkelman G, Jóhannesson G and Jónsson H 2000 Methods for finding saddle points and minimum energy paths *Progress on Theoretical Chemistry and Physics* ed S D Schwartz (Dordrecht: Kluwer–Academic)
[36] Nguyen-Manh D 2005 unpublished
Fu C-C and Willaime F 2005 unpublished
[37] Biersack J P and Ziegler J F 1982 *Nucl. Instrum. Methods* **141** 93
[38] Savrasov S Y 1996 *Phys. Rev.* B **54** 16470